Optics Letters

Shaping the spectral correlation of bi-photon quantum frequency combs by multi-frequency excitation of an SOI integrated nonlinear resonator

Alí M. Angulo,[1,2,*] Jan Heine,[1] J. S. S. Duran Gomez,[1] Hatam Mahmudlu,[1] Raktim Haldar,[1,2] Charalambos Klitis,[3] Marc Sorel,[3,4] and Michael Kues[1,2,5]

[1]Institute of Photonics, Leibniz University Hannover, Nienburger Str. 17, 30167 Hannover, Germany
[2]Cluster of Excellence PhoenixD (Photonic, Optics, and Engineering – Innovation Across Disciplines), Leibniz University Hannover, Hannover, Germany
[3]School of Engineering, University of Glasgow, Glasgow G12 8QQ, UK
[4]Institute of Technologies for Communication, Information and Perception (TeCIP), Sant'Anna School of Advanced Studies, Via Moruzzi 1, 56127 Pisa, Italy
[5]michael.kues@iop.uni-hannover.de
*ali.angulo@iop.uni-hannover.de

Received 21 August 2023; accepted 27 September 2023; posted 4 October 2023; published 19 October 2023

We reveal the generation of a broadband (> 1.9 THz) bi-photon quantum frequency comb (QFC) in a silicon-on-insulator (SOI) Fabry–Pérot micro-cavity and the control of its spectral correlation properties. Correlated photon pairs are generated through three spontaneous four-wave mixing (SFWM) processes by using a co-polarized bi-chromatic coherent input with power P_1 and P_2 on adjacent resonances of the nonlinear cavity. Adjusting the spectral power ratio $r = P_1/(P_1 + P_2)$ allows control over the influence of each process leading to an enhancement of the overall photon pair generation rate (PGR) $\mu(r)$ by a maximal factor of $\mu(r = 0.5)/\mu(r = 0) \approx 1.5$, compared to the overall PGR provided by a single-pump configuration with the same power budget. We demonstrate that the efficiency a_{ND} of the non-degenerate excitation SFWM process (NDP) doubles the efficiency $a_1 \approx a_2$ of the degenerate excitation SFWM processes (DP), showing a good agreement with the provided model.

https://doi.org/10.1364/OL.503909

The scalable practical generation and control of photonic quantum states will enable quantum signal and information processing for applications in quantum secured communications [1], quantum computing [2], quantum random number generation [3], and metrology beyond the classical limit [4]. In particular, correlated photon pairs generated inside a nonlinear cavity via SFWM processes contain a high number of equidistant frequency modes, forming large-scale high-dimensional quantum states [5,6], called QFCs. Such states are relevant for the implementation of quantum information processing and quantum communication [1]. Particularly, manipulating QFCs can lead to states with more complex structures, e.g., cluster states which are a key element for "one-way" quantum processing [7].

A strategy to generate more complex states is the consideration of several different superimposed SFWM processes in a single device which can enable the manipulation of the correlation characteristics by controlling the spatial properties [8,9], polarization [10], or the spectral distribution [11] of the input field. The efficiency of photon pair generation using a single-pump and dual-pump (non-degenerate) SFWM has been theoretically studied [12,13]. It was demonstrated that the PGR can be enhanced by tailoring the cavity resonance properties and the input field's spectral bandwidth: the energy is redistributed in the spectral domain in such a way that the generation is only allowed at the resonance frequencies of the cavity [12] in contrast to a non-cavity configuration. Furthermore, a bi-chromatic excitation configuration that induces two SFWM processes with different polarization states has been demonstrated in a microring resonator [10,14] leading to a single-photon seeded effect with additional induced frequency correlations. Moreover, a successful application of the pulsed dual-pump scheme resulted in the generation of squeezed light from a microring [15] and the formation of a nanophotonic molecule [16]. For both cases, an enhancement in the quality of the degenerated output squeezing was achieved by suppressing various parasitic nonlinear processes. These included a degenerate excitation process (DP), a non-degenerate excitation process (NDP), and a stimulated (seeded) FWM process that could occur even at low-power intensities, potentially leading to a parasitic cascaded FWM process [17]. The identification and control of these processes are fundamental to achieve high-quality quantum states, to enhance the quality of squeezing [15,16] and to avoid decoherence [18,19].

Our motivation is to investigate the controllable generation of high-dimensional quantum states by shaping the spectral correlations between the signal and the idler photon through a set of SFWM processes produced in a nonlinear integrated cavity. A rigorous study about the influence of multi-frequency excitation

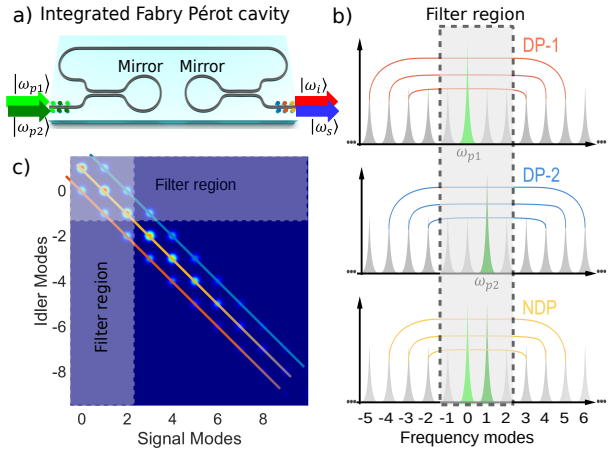

Fig. 1. (a) Scheme of the integrated cavity. In a bi-chromatic pump configuration, two photons from these fields are annihilated to generate a signal and an idler photon. (b) Representation of the three SFWM processes: in DP-1 (DP-2), two input photons with the same frequency $\omega_{p1,(p2)}$ are annihilated to produce a pair of correlated photons on frequency modes symmetrically located to the excitation frequency. In NDP, one photon with frequency ω_{p1} and another with frequency ω_{p2} are annihilated to produce a pair of correlated photons on frequency modes symmetrically located to the average frequency of the two input fields. (c) Calculated JSI with an arbitrary phase matching showing correlations between the first 10 signal and idler modes. Colored lines show the three sets of anti-correlated modes generated by the different processes DP-1 (red), DP-2 (blue), and NDP (yellow). A white-marked region indicates the spectral extent of the input field rejection filter.

on the spectral emission properties of the photon pairs has not been performed. In this work, we use a dual-frequency excitation field with variable intensities to investigate its effect on the photon pair spectral emission. This approach can be further extended to multiple-frequency input fields.

Exploiting a dual-pump configuration scheme in the third-order $\chi^{(3)}$ nonlinear SOI integrated Fabry–Pérot cavity [Fig. 1(a)], we generated a bi-photon QFC using two continuous wave input fields with power intensities below the threshold of parametric oscillation and centered at adjacent resonant frequencies of the cavity. The dual co-polarized input field excitation leads to the generation of three distinct sets of frequency anti-correlated modes through two DPs (DP-1 and DP-2) and one NDP process [Fig. 1(b)]. Fig. 1(c) shows a representation of the joint spectral intensity (JSI) which yields the spectral shape of the generated quantum state [11], revealing the correlations between the different frequency modes.

In our model, we consider two electromagnetic fields impinging on a $\chi^{(3)}$ nonlinear cavity with total power $P = P_1 + P_2$ and frequencies centered at the cavity resonances $\nu_j, j = 1, 2$, respectively; the DP-j with an efficiency a_j has a PGR $\mu_j(P_j) = a_j P_j^2$, while $\mu_{ND}(P_1, P_2) = 2a_{ND}P_1P_2$ accounts for the PGR of the corresponding NDP, which has twice the probability of occurrence of the DP case due to the presence of two input fields. Written in terms of the ratio $r = P_1/P$ and the total power P, the overall PGR ($\mu(r, P) = \mu_1(r, P) + \mu_{ND}(r, P) + \mu_2(r, P)$) is

$$\begin{aligned}\mu(r,P) &= a(r)P^2 \\ &= (a_1 r^2 + 2a_{ND}r(1-r) + a_2(1-r)^2)P^2,\end{aligned} \tag{1}$$

where $a(r)$ is the overall efficiency for a dual-pump that includes the three SFWM processes involved. Labeling the resonant cavity modes with integer numbers and choosing the frequency of the input fields centered at the modes 0 and 1, the quantum state generated at the output is

$$\begin{aligned}|\Psi\rangle = |vac\rangle + \eta[\sum_{m=0}(&\alpha_1^m|m\rangle_s|-m\rangle_i + \\ &+ \alpha_{ND}^m|m+1\rangle_s|-m\rangle_i + \alpha_2^m|m+1\rangle_s|-m+1\rangle_i)].\end{aligned} \tag{2}$$

Each term in Eq. (2) fulfills the corresponding energy conservation for the different processes. The state probabilities $|\alpha_x(r)|^2 = \mu_x(r, P)/\mu(r, P)$, with $x = 1, 2, ND$, define the generation probability of the correlated modes, i.e., the fractional contribution of each process to the overall generation. Each signal mode $|s\rangle_s$ has a detection correlation with three different idler modes that correspond to the DP-1, DP-2, and NDP processes. We can write the projection on this frequency mode as

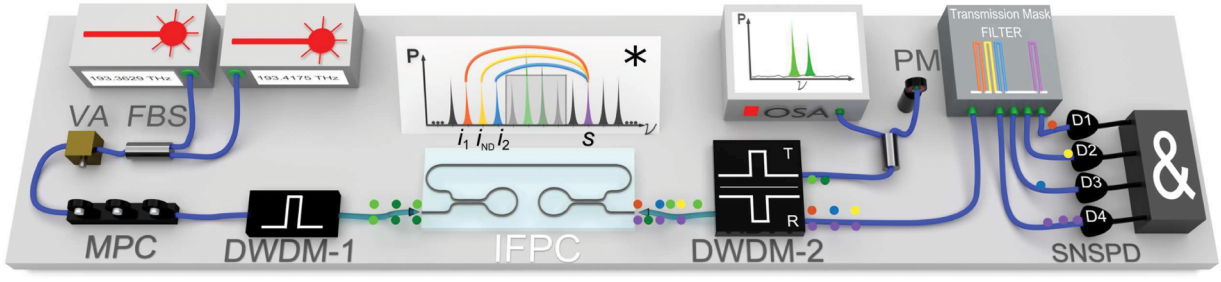

Fig. 2. Two fiber-coupled CW lasers with frequencies $\nu_1 = 193.363$ THz (light green) and $\nu_2 = 193.418$ THz (dark green) are superimposed at a 50:50 fiber beam splitter (FBS) and guided through a variable attenuator (VA) that controls the total power. A manual polarization controller (MPC) assures the TE_{00} mode, and a 100 GHz filter (DWDM-1) suppresses undesired laser frequency sidebands. The dual-frequency field is coupled into the cavity (IFPC) using a PM fiber lens. Two photons from this field are annihilated inside the cavity, and a photon pair (signal and idler) is generated through an NDP or DP. The output is coupled with a fiber lens and guided through a notch filter (200 GHz bandpass) (DWDM-2) centered at 193.4 THz. The remaining input field is guided through the transmission port and then splits to measure power (PM) and spectra (OSA) continuously, while the generated photons (represented as colored spheres) are guided through the reflected port to a programmable filter that separates the signal s (violet) and the three type of idler photons i_1 (red), i_{ND} (yellow), and i_2 (blue). Subsequently, coincidence measurements are performed using superconductive nanowire single-photon detectors (SNSPDs) and correlation measurements with a time-to-digital converter (5 ps resolution mode). Inset (*): correlations between s and i_1, and i_2 and i_{ND} modes are represented with colored lines according to the type of SFWM generation process; a gray rectangle encloses the frequencies blocked by the input field rejection filter.

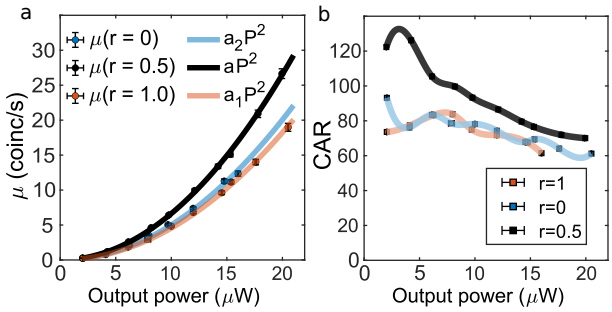

Fig. 3. (a) PGR as a function of the output power for $r = 0, 0.5, 1$. A quadratic function fit allows the calculation of the efficiencies for the single-input excitation cases ($a_1 = 4.55 \pm 0.03 \times 10^{10} cc/sW^2$, and $a_2 = 5.01 \pm 0.03 \times 10^{10} cc/sW^2$) and the dual-pump case ($a(r = 0.5) = 6.64 \pm 0.03 \times 10^{10} cc/sW^2$). (b) Measured CAR as a function of the output power for $r = 0, 0.5, 1$. The solid lines are spline curves used to guide the eye.

$$ {}_s\langle s|\Psi\rangle = (\alpha_1^s|-s\rangle_i + \alpha_{ND}^s|-(s-1)\rangle_i + \alpha_2^s|-(s-2)\rangle_i),, \quad \textbf{(3)} $$

where the values $|\alpha_x^s|^2 = \mu_x(r,P)/\mu^s(r,P)$ are proportional to the PGR output at the signal mode $|s\rangle_s$ for the process x and are normalized for each projection ($|\alpha_1^s|^2 + |\alpha_{ND}^s|^2 + |\alpha_2^s|^2 = 1$). To obtain the state coefficients in Eq. (3), we performed two experimental measurements: (M1) determining $\mu(r,P)$ for $r = 0, 0.5, 1.0$ to quantify $a(r)$ for the single- and dual-pump cases, and (M2) determining $\mu_x^s(r,P_0)$ at the power P_0, which allowed quantifying $|\alpha_x^s|^2$ at a spectral power ratio r.

A scheme of the experimental setup is shown in Fig. 2. For (M1) we used a transmission mask with two 1.5 THz bandwidth filters, each centered at 192.45 and 194.35 THz respectively, to separate the signal and idler photons and measure their time correlations with the detectors D1 and D2. For the special cases of $r = 0, 0.5, 1.0$, we measured the PGR $\mu(r,P)$ and coincidence to accidental ratio (CAR) following the method described in [20]. We fitted a quadratic function [Fig. 3(a)] to obtain the PGR efficiencies for the single-pump cases a_1 and a_2, respectively, and the overall efficiency $a(r = 0.5)$. We found that $a(r = 0.5) \approx 1.5a_{1,2}$, which demonstrates an overall enhancement of the PGR. The CAR value [Fig. 3(b)] for the dual-pump case ($r = 0.5$) reaches a maximum of 125 at around $5\,\mu W$. Each single-pump case ($r = 0, 1$) shows a lower CAR value. This demonstrates that for the double excitation, SFWM photon pairs are generated in a larger amount with respect to noise photons. Nevertheless, the ratio CAR($r = 0.5$)/CAR($r = 0$) diminishes from 1.6 at $5\,\mu W$ to 1.2 at $20\,\mu W$, showing a larger noise increment with higher powers. For (M2) the state probabilities $|\alpha_x^s|^2$ for $s = 5, \ldots, 40$ at a measured output power of $P_0 = 11\mu W$ were determined by performing three different coincidence measurements, specifically for the same signal frequency and the corresponding three different idler frequencies [(see Eq. (3)]. The signal/idler frequencies were resolved with 25 GHz bandwidth filters and then guided to four single-photon detectors (Fig. 2). The frequency channels sent to the three idler detectors were cyclically permuted. This allowed averaging the losses of the three idler detection paths. The different detection efficiencies and losses would otherwise influence the measurement outcomes. Measurements were conducted for 4 minutes per permutation cycle c for three cycles resulting in a total measurement time of 12 minutes per signal mode. The state probabilities determined from the projection ${}_s\langle s|\Psi\rangle$ were then calculated by $|\alpha_x^s|^2 \approx \sum_{c=1}^{3} \mu_{c,x}^s / \sum_{c=1}^{3} \sum_x \mu_{c,x}^s$

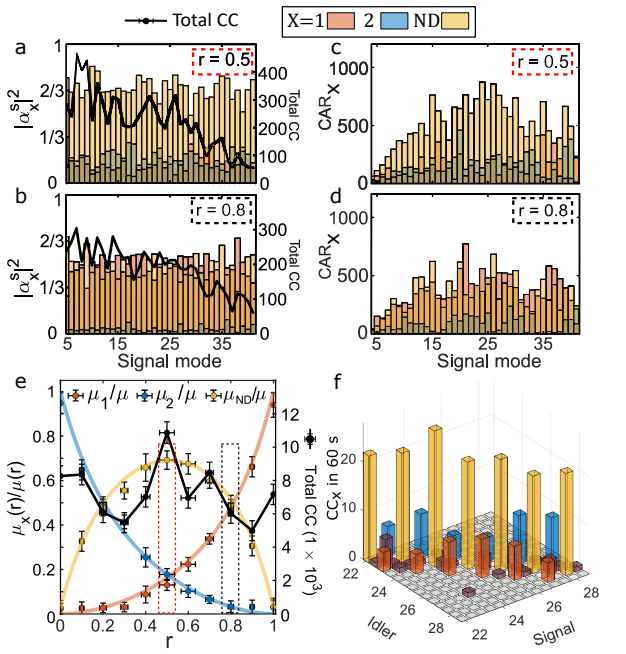

Fig. 4. State probabilities of the different x-SFWM processes at the signal mode s and measured total coincident counts (black line) are shown for (a) $r = 0.5$ and (b) $r = 0.8$. The corresponding measured CAR_x is shown in (c) and (d). In (e) the coincidence counts measured for each process normalized by the total coincidence counts are shown. A colored solid line shows a best fit with our model. A red and black rectangle encloses the measured values for $r = 0.5$ and 0.8, respectively. The error bars were calculated assuming a Poisson distribution. (f) JSI measured for the modes 22 to 29 with steps of 25 GHz corresponding to the half free-spectral range of the QFC showing no significant off-resonance photon pairs and no additional noise. For all cases in this figure, the colors correspond to the different x-SFWM processes: DP-1 (red), DP-2 (blue), and NDP (yellow).

with $x = 1, 2, ND$ and c as the number of the cycle. We performed this measurement for 35 signal modes and 11 different power ratios r. In Fig. 4 the measured total coincidence counts μ^s and the state probabilities $|\alpha_x^s|^2$ [Figs. 4(a) and 4(b)] with the corresponding CAR [Figs. 4(c) and 4(d)] for the cases ($r = 0.5$) and ($r = 0.8$) are shown. For $r = 0.5$ it can be observed that the PGRs for the DP-1 and DP-2 processes are nearly equal $\mu_1^s \approx \mu_2^s$, whereas the NDP process is approximately four times higher $\mu_{ND}^s \approx 4\mu_1^s$. For $r = 0.8$ it can be observed that the PGR for the DP-2 process goes to zero $\mu_2^s \approx 0$, and the PGR of the ND and the DP-1 processes are equal $\mu_{ND}^s \approx \mu_1^s$. This demonstrates our ability to tailor the JSI spectral shape and the influence of each process as a function of r. In both cases, the maximum CAR_x value is above 800, while for the frequency modes spectrally close to the input fields, a low value of <100 is observed, which is explainable by the leakage of the pump through the DWDM filter and Raman gain in Si [21]. In all considered cases, we observe a QFC bandwidth $\gtrsim$ 1.9 THz. The CAR values for a particular mode are greater than those measured in (M1); this is a consequence of the filter size that avoids noise outside our frequency region of interest. This effect can be applied to use the filtered idler mode as a high-quality heralded-single-photon source with the disadvantage of having lower PGRs [22]. To obtain the fraction of photon pairs $\mu_x(r,P_0)/\mu(r,P_0)$ generated

by each process [Fig. 4(e)], we integrated the coincidence counts over the 35-mode measurement for each r value for each process. Using the measured values for a_1 and a_2 obtained in (M1), a best fit was performed using our model, yielding the relative efficiency values $a_{ND}/a_1 = 2.03 \pm 0.07$, $a_2/a_1 = 1.10 \pm 0.01$, and $a(r = 0.5)/a_1 = 1.54 \pm 0.09$.

These values show a good agreement with our model [Eq. (1)] under the assumption that the efficiencies for the DP processes are equal $a_2 = a_1$ and the efficiency of the NDP process is $a_{ND} = 2a_1$. Substituting these values in Eq. (1), we find a dual-pump PGR enhancement factor of $a(r = 0.5)/a_1 = 1.5$, which agrees with our measurement and is also consistent with the previously measured efficiency values. The fact that a_{ND} is twice as much as the efficiency a_1 can be understood in terms of the set of SFWM continuous processes that form each DP and NDP: $\frac{\#NDPcontinuousprocesses}{\#DPcontinuousprocesses} = \frac{\sigma_1 \times \sigma_2}{\frac{1}{2}\sigma_2^2} = 2.0$, where $\sigma_{1,2}^2$ are the frequency bandwidths of the first and second laser source, respectively. We observe that in the range $0.2<r<0.8$, the NDP PGR is $\mu_{ND}>\mu_{1,2}$ showing a maximum at $r = 0.5$ where the PGR is four times higher than the PGR associated to the DP ($\mu_{ND} \approx 4\mu_{1,2}$). This behavior demonstrates that the NDP process has a main role in the photon pair generation in a multi-frequency excitation scheme. Independently, the off-diagonal and off-cavity resonance contributions were investigated by measuring a portion of the JSI in a 14×14 matrix [Fig. 4(f)]; there is no significant contribution on these spectral components by the used dual-pump scheme showing that the correlated photon pairs are generated just in the three diagonal lines defined by the three types of SFWM processes considered in our model.

We generated efficiently photon pairs [23] using a dual-pump configuration without observing the cascaded nonlinear interactions that usually occur in other platforms like silicon nitride [24] or AlGaAsOI [20]. The absence of a seeded effect can be explained by the high two-photon absorption present in SOI platforms. We thoroughly explored several dual-input field configurations varying the spectral power ratio r. We identified the generation of different spectral correlations in a bi-photon QFC generated through two DP and one NDP SFWM processes. We showed the availability to shape the correlations through the control of the influence of each process and successfully modeled this effect. We demonstrated that the efficiency $a_{ND} = 2.03a_1$ of the NDP process occurring in a dual-pump configuration is responsible for an overall PGR enhancement: $\mu(r = 0.5)/\mu(r = 0) = 1.54$.

These results represent a major step in understanding the generation mechanism of high-dimensional time-frequency states through the control of spectral correlations. Using synchronous, pulsed, higher-power input fields could lead to higher values of the PGRs from a multi-frequency excitation configuration and the creation of multiple bi-photons, simultaneously. Passing multiple photons correlated to each other through reconfigurable phase gates may enable the realization of more complex states, e.g., cluster states that can be applied to one-way quantum processing [1,7].

Funding. Deutsche Forschungsgemeinschaft (EXC 2122, Project ID 390833453); European Research Council [grant agreement no. 947603 (QFreC project)]; Bundesministerium für Bildung und Forschung (PQuMal, Quantum Futur Program); Alexander von Humboldt-Stiftung; Engineering and Physical Sciences Research Council (EP/P005624/1, EP/W035995/1).

Acknowledgment. R. H. acknowledges financial support provided by Alexander von Humboldt Stiftung to conduct the research.

Disclosures. The authors declare no conflicts of interest.

Data availability. Data underlying the results presented in this paper are not publicly available at this time but may be obtained from the authors upon reasonable request.

REFERENCES

1. M. Kues, C. Reimer, P. Roztocki, L. R. Cortés, S. Sciara, B. Wetzel, Y. Zhang, A. Cino, S. T. Chu, B. E. Little, D. J. Moss, L. Caspani, J. Aza na, and R. Morandotti, Nature **546**, 622 (2017).
2. N. Fabre, G. Maltese, F. Appas, S. Felicetti, A. Ketterer, A. Keller, T. Coudreau, F. Baboux, M. I. Amanti, S. Ducci, and P. Milman, Phys. Rev. A **102**, 012607 (2020).
3. Y. Okawachi, M. Yu, K. Luke, D. O. Carvalho, M. Lipson, and A. L. Gaeta, Opt. Lett. **41**, 4194 (2016).
4. S. K. Lee, N. S. Han, T. H. Yoon, and M. Cho, Commun. Phys. **1**, 51 (2018).
5. Y. J. Lu, R. L. Campbell, and Z. Y. Ou, Phys. Rev. Lett. **91**, 163602 (2003).
6. M. Kues, C. Reimer, J. M. Lukens, W. J. Munro, A. M. Weiner, D. J. Moss, and R. Morandotti, Nat. Photonics **13**, 170 (2019).
7. C. Reimer, S. Sciara, P. Roztocki, M. Islam, L. Romero Cortés, Y. Zhang, B. Fischer, S. Loranger, R. Kashyap, A. Cino, S. T. Chu, B. E. Little, D. J. Moss, L. Caspani, W. J. Munro, J. Azaña, M. Kues, and R. Morandotti, Nat. Phys. **15**, 148 (2019).
8. P. Boucher, H. Defienne, and S. Gigan, Opt. Lett. **46**, 4200 (2021).
9. D. Gutiérrez-López, M. Maldonado-Terrón, R. J. Hernández, V. Vicuña Hernández, R. Ramírez-Alarcón, H. Cruz-Ramírez, R. Jáuregui, and A. B. U'Ren, Phys. Rev. A **100**, 013802 (2019).
10. C. Reimer, M. Kues, L. Caspani, B. Wetzel, P. Roztocki, M. Clerici, Y. Jestin, M. Ferrera, M. Peccianti, A. Pasquazi, B. E. Little, S. T. Chu, D. J. Moss, and R. Morandotti, Nat. Commun. **6**, 8236 (2015).
11. K. Garay-Palmett, H. J. McGuinness, O. Cohen, J. S. Lundeen, R. Rangel-Rojo, A. B. U'Ren, M. G. Raymer, C. J. McKinstrie, S. Radic, and I. A. Walmsley, Opt. Express **15**, 14870 (2007).
12. K. Garay-Palmett, Y. Jeronimo-Moreno, and A. B. U'Ren, Laser Phys. **23**, 015201 (2013).
13. L. G. Helt, M. Liscidini, and J. E. Sipe, J. Opt. Soc. Am. B **29**, 2199 (2012).
14. Y. Zhang, M. Kues, P. Roztocki, C. Reimer, B. Fischer, B. MacLellan, A. Bisianov, U. Peschel, B. E. Little, S. T. Chu, D. J. Moss, L. Caspani, and R. Morandotti, Laser Photonics Rev. **14**, 2000128 (2020).
15. H. Seifoory, Z. Vernon, D. H. Mahler, M. Menotti, Y. Zhang, and J. E. Sipe, Phys. Rev. A **105**, 033524 (2022).
16. Y. Zhang, M. Menotti, K. Tan, V. D. Vaidya, D. H. Mahler, L. G. Helt, L. Zatti, M. Liscidini, B. Morrison, and Z. Vernon, Nat. Commun. **12**, 2233 (2021).
17. C. J. McKinstrie and M. G. Raymer, Opt. Express **14**, 9600 (2006).
18. L. Larger, A. Baylón-Fuentes, R. Martinenghi, V. S. Udaltsov, Y. K. Chembo, and M. Jacquot, Phys. Rev. X **7**, 011015 (2017).
19. S. Azzini, D. Grassani, M. Galli, L. C. Andreani, M. Sorel, M. J. Strain, L. G. Helt, J. E. Sipe, M. Liscidini, and D. Bajoni, Opt. Lett. **37**, 3807 (2012).
20. H. Mahmudlu, S. May, A. Angulo, M. Sorel, and M. Kues, Opt. Lett. **46**, 1061 (2021).
21. R. K. W. Lau, M. R. E. Lamont, Y. Okawachi, and A. L. Gaeta, Opt. Lett. **40**, 2778 (2015).
22. A. M. Branczyk, T. C. Ralph, W. Helwig, and C. Silberhorn, New J. Phys. **12**, 063001 (2010).
23. F. Mazeas, M. Traetta, M. Bentivegna, F. Kaiser, D. Aktas, W. Zhang, C. A. Ramos, L. A. Ngah, T. Lunghi, E. Picholle, N. Belabas-Plougonven, X. L. Roux, E. Cassan, D. Marris-Morini, L. Vivien, G. Sauder, L. Labonté, and S. Tanzilli, Opt. Express **24**, 28731 (2016).
24. Y. Okawachi, M. Yu, K. Luke, D. O. Carvalho, S. Ramelow, A. Farsi, M. Lipson, and A. L. Gaeta, Opt. Lett. **40**, 5267 (2015).